

Structural and short-time vibrational properties of colloidal glasses and supercooled liquids in the vicinity of the re-entrant glass transition

Cite as: J. Chem. Phys. 155, 074902 (2021); <https://doi.org/10.1063/5.0059084>

Submitted: 05 June 2021 . Accepted: 02 August 2021 . Published Online: 17 August 2021

 Xiaoguang Ma,  Chandan K. Mishra, P. Habdas, and  A. G. Yodh

COLLECTIONS

Paper published as part of the special topic on **Depletion Forces and Asakura-Oosawa Theory**



[View Online](#)



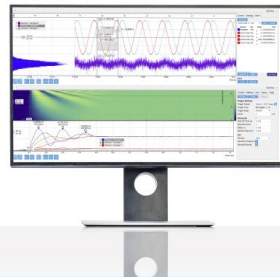
[Export Citation](#)



[CrossMark](#)

Challenge us.

What are your needs for
periodic signal detection?



Zurich
Instruments

Structural and short-time vibrational properties of colloidal glasses and supercooled liquids in the vicinity of the re-entrant glass transition

Cite as: *J. Chem. Phys.* **155**, 074902 (2021); doi: 10.1063/5.0059084

Submitted: 5 June 2021 • Accepted: 2 August 2021 •

Published Online: 17 August 2021



Xiaoguang Ma,^{1,2,a} Chandan K. Mishra,³ P. Habdas,⁴ and A. G. Yodh⁵

AFFILIATIONS

¹ Center for Complex Flows and Soft Matter Research, Southern University of Science and Technology, Shenzhen, Guangdong 518055, China

² Department of Physics, Southern University of Science and Technology, Shenzhen, Guangdong 518055, China

³ Discipline of Physics, Indian Institute of Technology (IIT) Gandhinagar Palaj, Gandhinagar, Gujarat 382355, India

⁴ Department of Physics, Saint Joseph's University, Philadelphia, Pennsylvania 19131, USA

⁵ Department of Physics and Astronomy, University of Pennsylvania, Philadelphia, Pennsylvania 19104, USA

Note: This paper is part of the JCP Special Topic on Depletion Forces and Asakura–Oosawa Theory.

^a Author to whom correspondence should be addressed: maxg@sustech.edu.cn

ABSTRACT

We investigate the short-time vibrational properties and structure of two-dimensional, bidisperse, colloidal glasses and supercooled liquids in the vicinity of the re-entrant glass transition, as a function of interparticle depletion attraction strength. The long-time spatiotemporal dynamics of the samples are measured to be non-monotonic, confirming that the suspensions evolve from repulsive glass to supercooled liquid to attractive glass with increasing depletion attraction. Here, we search for vibrational signatures of the re-entrant behavior in the short-time spatiotemporal dynamics, i.e., dynamics associated with particle motion inside its nearest-neighbor cage. Interestingly, we observe that the anharmonicity of these in-cage vibrations varies non-monotonically with increasing attraction strength, consistent with the non-monotonic long-time structural relaxation dynamics of the re-entrant glass. We also extract effective spring constants between neighboring particles; we find that spring stiffness involving small particles also varies non-monotonically with increasing attraction strength, while stiffness between large particles increases monotonically. Last, from study of depletion-dependent local structure and vibration participation fractions, we gain microscopic insight into the particle-size-dependent contributions to short-time vibrational modes in the glass and supercooled liquid states.

Published under an exclusive license by AIP Publishing. <https://doi.org/10.1063/5.0059084>

I. INTRODUCTION

The re-entrant glass transition is a remarkable phenomenon wherein a continuous increase in the attractive force between constituent particles first causes a glass to melt and then drives the resultant liquid to evolve into a glass again. These transitions, from repulsive glass to liquid to attractive glass, and their associated spatiotemporal dynamics, are strikingly non-monotonic with respect to attraction strength. The re-entrance effect has been experimentally observed in a range of colloidal systems,^{1–10} and theoretical calculations suggest that the effect arises from a subtle interplay of volume fraction (ϕ) and short-range attraction

strength.^{2,3,11,12} To date, most insight into the re-entrance phenomenon derives from the measurements of *long-time* spatiotemporal dynamics.^{1,2,5,10,13} Here, we experimentally investigate the same general class of samples, but we focus on particle trajectories at short time scales, i.e., on time scales wherein the sample is metastable and its constituents do not escape from their nearest-neighbor cages. These within-cage particle trajectories are loosely connected to the high-frequency viscoelastic response of the colloidal suspensions; they offer an unexplored (short-time) window for insight into the re-entrance phenomena, potentially linking in-cage particle fluctuations to cage-breaking particle rearrangements.^{14–16}

To carry out this work, we employ two-dimensional (2D), bidisperse, colloidal suspensions in a background solvent consisting of water and small surfactant micelles made from hexaethylene glycol monododecyl ether ($C_{12}E_6$). The micelles induce a depletion force between the particles^{17,18} that can be tuned. Depletion attraction is a well-known entropic force that has been directly measured^{19–26} and utilized extensively to control the assembly, structure, and dynamical behavior of colloids.^{1,2,4,5,27–43} Notably, in most re-entrant glass experiments,^{1,2,5,8,10} small polymers were added to the suspension to vary the depletion attraction between particles, i.e., by varying polymer concentration (c_p). In our experiments, the depletion attraction strength is induced by rod-like $C_{12}E_6$ micelles whose length can be temperature-tuned.^{20,24,26,43,44} The temperature-dependent length of the rod-like micelles provides a convenient “knob” for controlling attraction strength *in situ*. Thus, with an appropriate sample volume fraction (ϕ), we can change the sample state from repulsive glass to liquid to attractive glass, simply by varying temperature.

Previously, re-entrant glass transitions have been reported in 2D and 3D colloids with monodisperse or slightly polydisperse particle distributions. For example, 2D colloids composed of monodisperse ellipsoidal particles exhibit a transition from repulsive glass to liquid facilitated by the formation of quasi-nematic domains at intermediate attraction strength.^{5,6} The ellipsoids inside these domains have increased orientational order, which releases volume to the system so that particles (on average) diffuse more freely. By contrast, in 3D colloidal suspensions of spheres, a slight polydispersity (about 5%) is required to avoid crystallization; local ordered domains have never been observed in these systems during the re-entrance process.^{1,2,8,10}

Our 2D *bidisperse* colloids differ qualitatively from the samples employed to date in re-entrance phenomena research, and to our knowledge, the present experiments are the first to report re-entrant glass transition behavior with this system. Investigation of *bidisperse* colloids offers an opportunity to explore the influence of polydispersity in a new context. Specifically, because depletion forces depend sensitively on the particle diameter, the large and small constituent particle species experience substantially different depletion interactions; as a result, the sample microstructure and dynamics associated with the transition phenomenon differ from those of the previous work on re-entrance and differ from polydisperse and bidisperse colloidal glasses with pure repulsive interactions.^{45,46} Moreover, the 2D colloids facilitate rapid whole-sample video recordings of fast dynamics, a feature crucial for studying short-time (in-cage) vibrations.^{14–16}

In the experiments, we measure the mean-square-displacement (MSD) and the self-intermediate scattering functions of the samples by video microscopy. Their long-time behavior defines the state of each sample, i.e., repulsive glass, supercooled liquid, and attractive glass, at temperatures $T = 22, 28$, and $34\text{ }^\circ\text{C}$, respectively. To study particle trajectories on short time scales, we carry out video microscopy at high frame rates. From these high-frame-rate image trains, we compute the vibrational modes and effective spring networks of the metastable samples based on the covariance of the particle displacements.^{47–51} Covariance matrix techniques are well understood and have been widely used in the colloid community to study the vibrational mode structure and the vibrational density of states (DOS) of colloidal glasses,^{48,49,52,53} gels,⁴¹

clusters,⁵⁴ and crystals.^{50,55–58} Covariance matrix methods have also been utilized to establish a connection between quasi-localized low-frequency modes and particle rearrangement events,^{49,59,60} as well as to probe active matter,⁶¹ granular systems,⁶² and far-from-equilibrium assemblies.⁶³ In our experiments, on the shortest time scales, the modes in the two glass states are harmonic, but the modes in the supercooled liquid state exhibit a hint of anharmonicity that grows with increasing observation time scale. From the analysis of these short-time harmonic modes, we determine the effective spring constants between particles, k_{eff} , the vibrational density of states, the particle participation fractions in each mode, $P_F(\omega)$, and the mode participation ratios, $P_r(\omega)$, which classifies the modes as extended or localized. We investigate all of these properties as functions of depletion attraction strength and particle size.

Interestingly, features such as the vibrational mode anharmonicity exhibit non-monotonic dependence with increasing depletion attraction strength, similar to the sample’s long-time spatiotemporal dynamics. Other short-time-derived parameters exhibit particle-size-dependent trends. For example, the nearest-neighbor pair correlation function and the effective spring constants (k_{eff}) associated with small particles have non-monotonic dependence with increasing depletion interactions; by contrast, the k_{eff} between the large particles become monotonically stiffer with increased depletion attraction. Size-dependent contributions from different particle types were also observed in the particle participation fractions. Large particles contribute more to low-frequency modes in the repulsive glass; small particles dominate the low-frequency modes in the attractive glass; large and small particles contribute roughly equally to the modes of the supercooled liquid state. Finally, at our packing fractions, the mean interparticle separation between small particles increases monotonically with increasing depletion attraction, which differs qualitatively from that of the large-large and large-small interparticle separation. To our knowledge, this microstructural behavior has not been reported and helps us to understand this depletion-driven system better.

The remainder of this paper is organized as follows: In Sec. II, we describe sample preparation, characteristics, and observation techniques. Then, in Sec. III, we sequentially report on and discuss the sample structure, sample long-time spatiotemporal dynamics and, most extensively, sample vibrational modes and related properties. Associated analysis tools, definitions, and procedures, such as the displacement covariance technique, are provided in relevant sub-sections. Finally, we summarize the results, and we discuss implications and potential future studies.

II. EXPERIMENT

The experiments employ a 44 mM aqueous solution of $C_{12}E_6$ surfactant molecules. At this concentration, $C_{12}E_6$ molecules self-assemble into rod-like micelles. The cross sectional diameter of these micelle rods is about 4.3 nm, and the average length of these rods grows from 19 nm at $22\text{ }^\circ\text{C}$ to 31 nm at $28\text{ }^\circ\text{C}$.^{24,26} This effect has been utilized to tune interparticle attractive forces in colloidal suspensions *in situ*.^{42–44}

For the particles, we use carboxylated polystyrene latex beads (Thermo Scientific) with two different sizes. The small and large particles have nominal diameters, $\sigma_s = 1.0\text{ }\mu\text{m}$ and $\sigma_l = 1.4\text{ }\mu\text{m}$, and

polydispersities, 1.5% and 1.1%, respectively. For sample preparation, we suspend the received particle solution in deionized (DI) water and remove the residual impurities and aggregates by repeated centrifugations (up to ten times). The two cleaned particle solutions are then mixed together; the number ratio between the large and small species is kept close to 1:1 in the resultant suspension. Finally, the solvent (DI water) is replaced by the 44 mM $C_{12}E_6$ surfactant solution via repeated centrifugations.

The depletion interactions were characterized in a separate experiment.⁴³ We defined the strength of the depletion forces by the minimum value, $-\Delta U$, of the pair potential, $U(r)$, which is measured as a function of interparticle separation, r , in dilute suspensions (e.g., area packing fraction $\phi < 0.005$). Figure 1(a) shows $-\Delta U$ for the small particles ($\sigma_s = 1.0 \mu\text{m}$) vs T ; more details about the measurement can be found in Ref. 43. In dense colloidal suspensions, many-body interactions between particles are important, and it is difficult to extract the true pair-wise ΔU . Herein, we will assume that the ΔU dependence on T is qualitatively the same in the dilute and dense particle packings, and we will use T to characterize the relative depletion-induced attraction strength.^{42,43} A similar approximate approach was adopted in previous

experiments on the re-entrant glass transition wherein the polymer concentration is used for characterizing the relative depletion effect.^{1,2,5,6}

Wedge cells are used to create a large two-dimensional (2D) domain of a densely packed colloidal suspension. The procedure for making the wedge cell has been described previously.⁴² Briefly, we inject 10 μl of the prepared sample solution (10% in volume fraction) into the wedge using a precision pipette. Once loaded, the sample solution quickly fills the wedge gap via capillary forces. We seal the wedge cell peripherally with a UV glue (Norland 65). The finished sample cell is then placed vertically on the bench to enable colloidal particles to settle to the wedge side (driven by gravity). This process typically lasts from 24 to 36 h. During this waiting period, the particles gradually form a densely packed monolayer near the wedge. Then, the wedge cell is placed on the stage of an inverted microscope (Zeiss Axiovert 135) [Fig. 1(b)]. The sample is imaged through a 100 \times oil-immersion objective (NA = 1.3) with an additional 2.5 \times optical magnifier. Within the field-of-view (about $70 \times 60 \mu\text{m}^2$), the colloid can be regarded as being confined by two parallel walls. The area packing fraction of the sample is $\phi = \pi(N_s \sigma_s^2 + N_l \sigma_l^2)/(4A)$, where $N_s = 1200$ and $N_l = 1200$ are the respective numbers of small and large particles that occupy an area A ; in this experiment, $\phi \approx 0.80$.

The sample temperature is maintained by using an objective heater (PeCon GmbH) ranging from $T = 22$ to 34°C . Movies of particle motion within the field-of-view are recorded under bright-field illumination at a resolution of $1280 \times 1024 \text{ pixel}^2$ using a monochrome CMOS camera (EoSens Mini, Mikrotron). At each T , we first wait 30 min to permit the colloidal sample to equilibrate and reach a metastable state. After that, we first record a 3-h video at 2 fps, and then, we record another 5-min video at 200 fps. The 3-h video is used to investigate long-time structural relaxation, and the 5-min video is analyzed to extract short-time vibrational properties. During the experiment, we do not observe changes in the sample area packing fraction, and the majority of particles (except those close to borders) stay within the field-of-view throughout the experiment.

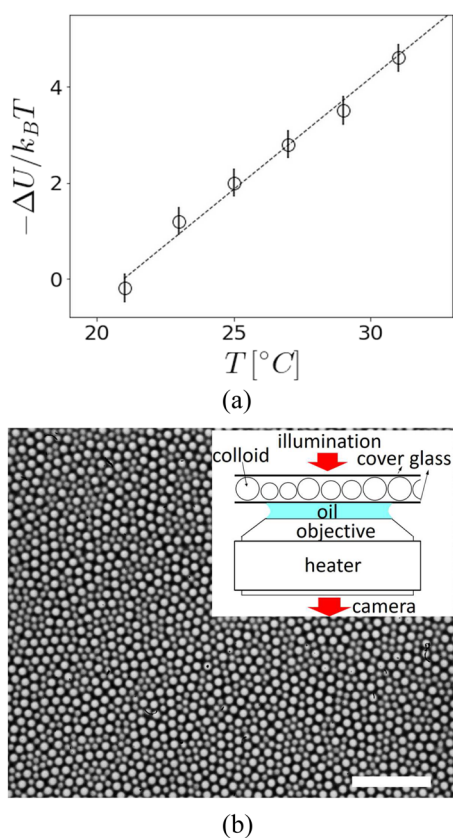


FIG. 1. (a) Interparticle attraction strength, $-\Delta U/k_B T$, vs T measured in a dilute colloidal suspension. Here, k_B is the Boltzmann constant. The dashed line is a linear fit to the data. (b) Optical microscopy image of the 2D colloidal sample. The scale bar is $10 \mu\text{m}$. Inset: schematic of the experimental setup.

III. RESULTS AND DISCUSSION

A. Sample structure

We characterize the static structure of the sample at different T using the pair correlation function, $g(r)$. Figure 2 shows $g(r)$ at $T = 22, 28$, and 34°C ; note, for clarity, that data from only three T 's are shown. At the first glance, the $g(r)$ seemed almost identical at all three T 's, especially at long separation (e.g., $r/\sigma_s > 2$). The first three $g(r)$ peaks, arising at $r/\sigma_s \approx 1$, $r/\sigma_s \approx 1.2$, and $r/\sigma_s \approx 1.4$, represent the nearest-neighbor correlations of small–small, small–large, and large–large particle pairs, respectively. These peaks exhibit subtle variations across the three T 's. Within our experimental resolution, the peaks related to large particles show minimal changes with increasing T . The large–large $g(r)$ peak height is identical for all three T 's; the peak location decreases slightly when temperature increases from $T = 22$ to 28°C , but thereafter, the peak location does not change anymore [Fig. 2(b)]. By contrast, the $g(r)$ peaks for the small–small particle pairs exhibit more notable changes [Fig. 2(c)]. To quantify the variations, we fit $g(r)$ near its peak position

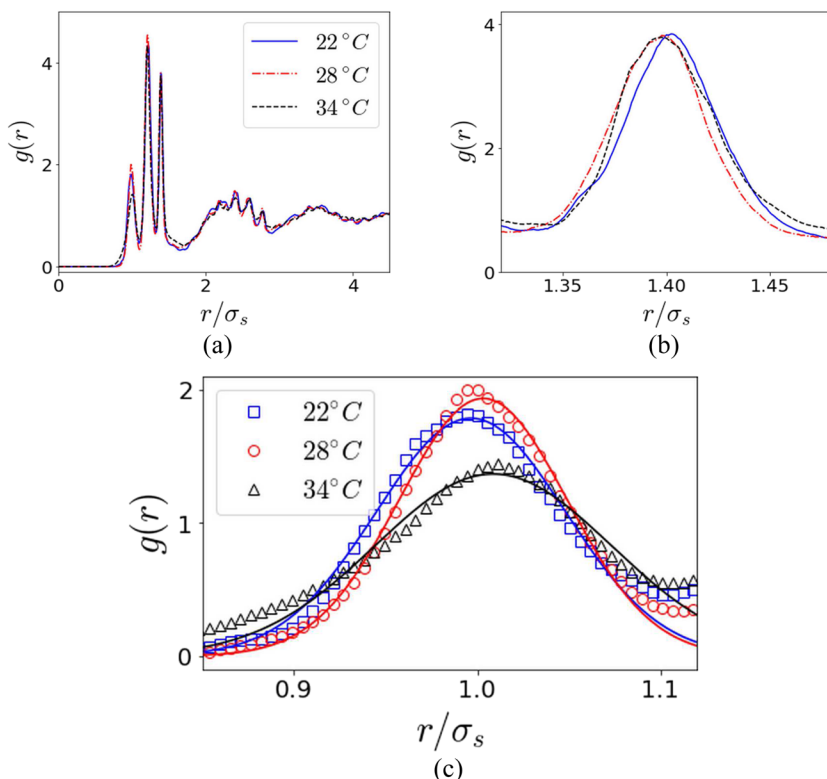


FIG. 2. (a) Pair correlation function, $g(r)$, vs interparticle separation, r , at $T = 22, 28$, and 34°C ; r is normalized by the small-particle diameter σ_s . (b) Enlarged $g(r)$ peaks for large-large particle correlations shown with the same colors as in (a). (c) Enlarged $g(r)$ peaks for small-small particle correlations shown with the same colors as in (a). The solid lines are best Gaussian fits to data (see the main text). The fitted peak heights, peak positions, and half-widths are $g^* = 1.79 \pm 0.01$, 1.93 ± 0.01 , and 1.37 ± 0.01 ; $\mu/\sigma_s = 0.997 \pm 0.0004$, 1.003 ± 0.0003 , and 1.09 ± 0.0004 ; and $\delta/\sigma_s = 0.052 \pm 0.0004$, 0.046 ± 0.0002 , and 0.064 ± 0.0005 at $T = 22, 28$, and 34°C , respectively.

($r/\sigma_s \approx 1$) by the Gaussian function, $g(r) = g^* \exp[-(r - \mu)^2/(2\delta^2)]$. The Fig. 2 caption reports g^* (peak height), μ/σ_s (peak position), and δ/σ_s (peak half-width) at $T = 22, 28$, and 34°C , respectively.

The fitted μ suggests that the mean separation between small particles and their small-particle neighbors *increases* with increasing depletion attraction strength. Evidently, there is more free volume in small-particle-rich regions at higher T 's wherein the depletion attraction is stronger. By contrast, the number of small-particle nearest neighbors, quantified by the peak height, g^* , and by its standard deviation, δ , exhibits *non-monotonic* dependence with increasing depletion attraction strength.

This particle-size-dependent increase in mean separation with increased depletion attraction strength is important, and to our knowledge, it has not been reported. Experiments with 3D colloidal suspensions did not see this effect, likely because they used particles with a small polydispersity (>5%) and because it is difficult to differentiate amongst different particle sizes when employing ensemble-averaged scattering measurements.³⁴ Moreover, in our prior work on 2D bidisperse colloidal glasses with larger $\phi \approx 0.82$, the first three $g(r)$ peaks for small-small, small-large, and large-large particle correlations remained the same across all T 's, suggesting that increased attraction did not change local particle arrangements.⁴² By contrast, our work on 2D bidisperse colloidal fluids (with smaller $\phi < 0.7$), found that the mean separations between nearest neighbors were always reduced with increasing short-range attractive forces.⁴³ Based on the ϕ dependence of these prior observations, one might conclude that the

effects of increased short-range attractive forces on pair correlations tend to diminish at large ϕ . However, in our present sample ($\phi \approx 0.80$), although the large-large particle correlations stop responding to the increased depletion attraction strength, the small-small particle correlations do not. We surmise that $\phi \approx 0.80$ is close to a threshold packing fraction for the sample as whole, ϕ_{th} , beyond which the attractive forces no longer affect the shapes and positions of the $g(r)$ peaks. Note, most generally, that it is possible that ϕ_{th} for the large particles is different (and lower) than that for the small particles.

A plausible contributing cause for this particle-size-dependent $g(r)$ phenomenon stems from the comparatively stronger depletion potential energy minima between large-large and large-small particle pairs compared to those between small-small particle pairs. In particular, with the same depletants in the background solution, particles with larger diameters will experience a comparatively stronger depletion attraction strength ($-\Delta U$) that grows linearly with particle diameter.^{17,19} Additionally, other recent findings also suggest that large particles in dense polydisperse systems are more arrested than small ones in the same environment.^{45,46}

We offer the following speculations to explain these microstructural observations. The large particles are driven to pack close to one another by the relatively strong depletion force; in this situation, the large-large particle correlations (and effective spring constants) are predominantly determined by their short-range repulsive (hard-sphere-like) interactions. The situation for the small particles is more complex because, in addition to the

changing depletion attraction between the small particles, the local environment around the small particles depends on confinement by the large particles. For example, if the large particles are preferentially brought together (toward close-packing) by increasing depletion attraction, then the small particles have more local space to explore, and the mean separation of small–small particle pairs could actually increase in the bidisperse suspensions. This subtle effect in the bidisperse colloid, which brings about an increased local free volume for the small particles, will compete with the temperature-dependent increase of depletion attraction between small particles. The interplay of competing effects contributes to the re-entrance phenomenology of the *bidisperse* colloids at a high packing fraction.

Note, here that we have restricted our structural analysis to pair-wise (two-body) correlations, because they are the dominant indicator of sample disorder. Indeed, the two-body excess entropy derived from particle pair correlation functions has been shown to account for greater than 90% of the total excess entropy in typical liquids.⁶⁴ Nevertheless, the increased depletion strength in our experiments can influence short-range order beyond pair correlations. Such effects have been reported in a bidisperse colloidal experiment, for example, wherein three-body correlations among the large particle species diminish as the concentration of the small-particle species (deplentants, in this case) slightly increase over a narrow concentration range.^{65,66} On the other hand, two-body correlations in the same samples were not observed to vary for the same small-particle species concentration change. Clearly, structural analysis involving more than two particles should be carried out in future work to fully understand the structural impact of increasing depletion forces.

B. Long-time relaxation dynamics

The state of our sample, e.g., glass or liquid, is most accurately identified from its long-time spatiotemporal behavior. To this end, we measure the MSD, $\langle \Delta r^2(\tau) \rangle$, and the self-intermediate scattering function, $F_s(\tau) = \frac{1}{N} \langle \sum_{j=1}^N \exp[i \frac{2\pi}{\sigma_s} \Delta r_j(\tau)] \rangle$, over times ranging from 0.5 to 10^4 s. Here, $\Delta r(\tau) = |\vec{r}(t_0 + \tau) - \vec{r}(t_0)|$, t_0 is an arbitrary initial time, and N is the total number of particles. The brackets, $\langle \dots \rangle$, represent a time average over the entire trajectory length. To remove the Mermin–Wagner fluctuations often found in 2D samples, we use cage-relative particle displacement Δr_{cr} in the place of Δr in the above formulas following Refs. 67 and 68. Note that MSD and $F_s(\tau)$ computed from Δr_{cr} and Δr show the same qualitative dependence with increasing temperature, i.e., the sample states do not depend on removal of cage-relative motions. Hereafter, we will describe the system with the cage-relative MSD and $F_s(\tau)$.

Figure 3(a) shows the measured cage-relative MSDs vs lag time, τ , at five temperatures ranging from $T = 22$ to 34 °C. The MSDs are normalized by the squared small-particle diameter, σ_s^2 . At $T = 22$ °C, the MSD is almost flat for more than four orders of magnitude in τ . This is typical MSD behavior for glasses, when the MSD arises mainly from particle displacement fluctuations within cages formed by neighboring particles. We call the sample at $T = 22$ °C a repulsive glass, because the depletion attraction strength at this temperature is close to zero [see Fig. 1(a)], leaving only the hard-sphere-like short-range repulsive interaction between all particles. At $T = 25$ °C, the MSD curve rises sharply at long times ($\tau > 10^3$ s); this increase

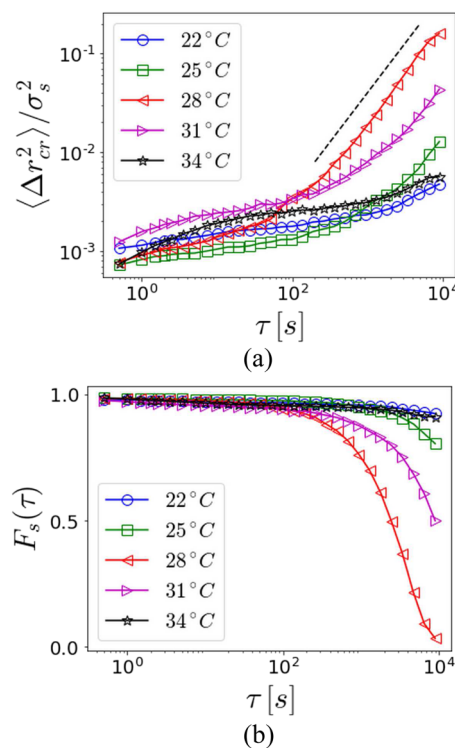


FIG. 3. (a) Cage-relative MSD, $\langle \Delta r_{cr}^2(\tau) \rangle$, vs τ at five different T 's; $\langle \Delta r_{cr}^2(\tau) \rangle$ is normalized by the square of the small-particle diameter, σ_s^2 . The black dashed line has a unit slope. (b) Self-intermediate scattering function, $F_s(\tau)$, vs τ at the same T 's as in (a).

suggests that the sample is in a less arrested state than that of the repulsive glass at 22 °C. At $T = 28$ °C, the long-time MSD exhibits fairly normal diffusion behavior with a unit slope. This MSD behavior confirms that the colloidal sample fully relaxes within the experiment duration. In other words, at 28 °C, the sample is a supercooled liquid. When the sample temperature is further increased to 31 °C, the liquid-like sample becomes more arrested. At the highest temperature, $T = 34$ °C, the MSD becomes very similar to those of the repulsive glasses. We call the sample at 34 °C an attractive glass; at this temperature, the depletion attraction has its largest value [see Fig. 1(a)]. Clearly, with increasing temperature, or equivalently increasing depletion attraction strength, the repulsive glass sample first melts into a supercooled liquid and then refreezes into an attractive glass. Thus, these phenomena manifest all characteristics of the re-entrant glass transition.¹² Note again that we also measured the *normal* MSDs using Δr ; the normal MSDs are greater than the cage-relative MSDs at all T 's (due to Mermin–Wagner fluctuations), but they exhibit the same re-entrance behavior (see the [supplementary material](#)).

To further corroborate that our sample exhibits a re-entrant glass transition, we compare the cage-relative $F_s(\tau)$ at different T 's in Fig. 3(b). At the lowest (22 °C) and highest (34 °C) temperatures, the $F_s(\tau)$ are almost flat across the full range of τ , showing that the system is fully arrested; the particles hardly move away from their

initial positions at these T 's. These $F_s(\tau)$ verify that the sample is in repulsive and attractive glass states at $T = 22$ and 34 °C, respectively. At $T = 28$ °C, however, $F_s(\tau)$ rapidly decays to $1/e$ in $\sim 3 \times 10^3$ s, thereby exhibiting the liquid-like character of the system. Note that the normal $F_s(\tau)$ decays faster than the cage-relative $F_s(\tau)$, making the sample look less arrested. Nevertheless, the normal $F_s(\tau)$ also exhibits a non-monotonic trend with increasing T . Thus, both the MSD and the $F_s(\tau)$ data confirm that our sample experiences a re-entrant glass transition as a function of increasing short-range depletion attraction strength.

Another important observation, apparent from the measurements of long-time dynamics, is that at short times ($\tau < 100$ s), the MSD and $F_s(\tau)$ data are flat for all T 's. This unchanging dynamical behavior is mainly due to strongly confined in-cage particle displacement fluctuations. These small displacement fluctuations at short times resemble those in solid-like states of matter (both stable and metastable states).

We focus next on short-time dynamical behaviors. These short-time behaviors have not been studied in the context of re-entrance. We will examine the vibrational properties of the sample in solid-like stable and metastable states spanned by the re-entrance phenomenon. Please note that analyses in the remaining sections, i.e., the vibrational analyses, are carried out using experimental videos recorded at 200 fps.

C. Vibrational modes and mode anharmonicity

To derive the short-time vibrational properties for N particles in 2D, we first compute a displacement vector $\vec{u} = \{u_1, u_2, \dots, u_{2N}\}$ at time t for the $2N$ degrees of freedom associated with the particles in the sample; we use the first and second N elements in \vec{u} to denote particle displacements along the x - and y -axis, respectively, following Refs. 48, 49, and 52. For example, the i th ($i \in \{1, 2, \dots, N\}$) particle contributes two elements to \vec{u} , namely, the components $u_i(t) = x_i(t) - \langle x_i(t) \rangle$ and $u_{N+i}(t) = y_i(t) - \langle y_i(t) \rangle$; here, $\langle \dots \rangle$ indicates a time average, and $\langle x_i(t) \rangle$ ($\langle y_i(t) \rangle$) is the equilibrium position for the i th particle along the x -axis (y -axis). We then compute the $2N \times 2N$ displacement covariance matrix, $C_{nn'} = \langle u_n(t)u_{n'}(t) \rangle$ ($n, n' \in \{1, 2, \dots, 2N\}$). In the harmonic approximation, the covariance matrix, C , the stiffness matrix, K , and the dynamical matrix, D , are closely related. They describe physics in the so-called “shadow” colloidal suspension that has the same equilibrium particle positions and the same potentials (harmonic springs) between particles as in the experimental sample, but with zero viscous damping.^{49,51,53,55,58,59,69}

The dynamical matrix, D , characterizes the vibrational modes of the “shadow” system. For a system of identical particles, $D = K/m = k_B T C^{-1}/m$, where m is the particle mass. Our system is composed of two types of particles; the small and large particles have masses m_s and m_l , respectively. In this case, $D_{nn'} = k_{nn'}/\sqrt{m_s m_l}$, where m_i and m_j are the actual particle masses (m_s or m_l) associated with the matrix element index (n and n'). The eigenvalues of D are the squared angular frequencies (ω^2) of the sample vibrational modes, and the corresponding $2N$ -dimensional eigenvector, $\vec{e}(\omega)$, represents the displacement amplitudes of the particles oscillating in the mode at frequency ω .

The conversion of C to K and D is rigorous when the system is in thermal equilibrium, and the equipartition theorem can be

applied. In practice, this requirement can be relaxed as long as the sample is in a metastable state wherein the equipartition condition still holds.^{48,49,51,52} Since we seek to apply this formalism, it is important to first verify the equipartition assumption before interpreting results. We do this by testing for anharmonicity and confirming the absence of rearrangement events. To this end, we follow Ref. 52 and quantify anharmonic effects under our full range of experimental conditions.

We first compute D and its associated eigenmodes. Then, we examine each mode for anharmonic effects. Specifically, we project the time-dependent, $2N$ -dimensional displacement vector, \vec{u} , onto each eigenvector, $\vec{e}(\omega)$; this projection yields the eigenmode projection coefficient, $c_\omega(t)$, as a function of time t , i.e., $c_\omega(t) = \vec{u}(t) \cdot \vec{e}(\omega)$. The potential energy of the system is $V[\vec{u}(t)] = \vec{u}(t)K\vec{u}(t)^* \propto \sum_\omega [c_\omega(t)]^2$. Note that the energy contribution of the mode at frequency ω is $E_\omega \propto \omega^2 c_\omega(t)^2$. Equilibrium statistical mechanics requires that $E_\omega(t) \sim \exp(-\omega^2 c_\omega(t)^2/(2k_B T))$ [see Fig. 4(a)].

Deviations of $c_\omega(t)$ from the Gaussian distribution quantify anharmonicity associated with the eigenmode. Previously, the well-known non-Gaussian parameter (or excess kurtosis), $\alpha_2(\omega) = \langle c_\omega^4(t) \rangle / (3\langle c_\omega(t)^2 \rangle^2) - 1$, was used for quantifying mode anharmonicity.⁵² Vibrational modes with $\alpha_2 < 0.2$ can be safely assumed to be harmonic and can be used for the computation of K and D . We will employ the same method for mode characterization in the present work.

At short times ($\tau < 300$ s), the sample MSD and $F_s(\tau)$ exhibit plateau behavior at all T 's. This behavior indicates that the samples are in solid-like metastable states. Nevertheless, to ameliorate all possible effects of long-time structural relaxation, we restrict our analyses of K and D to short-time metastable states only; this is done by using particle trajectories collected over times that are much shorter than those of the long-time structural relaxation time.^{41,51,70} Additionally, as a further check, we systematically examine mode anharmonicity as a function of trajectory duration, i.e., by monitoring c_ω and the corresponding $\alpha_2(\omega)$. In this way, we identify the short-time durations for which the harmonic approximation is satisfied, and we only utilize these trajectories for the analysis. Note that one can also identify anharmonicity using individual particle displacements;⁵¹ the two methods are equivalent.

Figure 4(b) shows an example of the non-Gaussian parameter, $\alpha_2(\omega)$, vs mode frequency, ω . The result is obtained from the supercooled liquid sample at $T = 28$ °C, which is expected to be the most anharmonic. The experimental time duration used for this calculation is 50 s. As shown in Fig. 4(b), a vast majority of modes in the supercooled liquid are harmonic with $|\alpha_2| < 0.2$. A handful modes (<40 modes) in the lowest and highest frequency ranges, however, show slight anharmonicity; to be safe, these modes are excluded from subsequent analyses. Note that these anharmonic modes often result from rattling particles and from tiny shifts of equilibrium positions during experiment.^{51,52,70} Since $\alpha_2(\omega)$ fluctuates around zero, we compute the standard deviation, $\delta\alpha_2$, of the non-Gaussian parameter for all modes, and we use $\delta\alpha_2$ to systematically characterize overall anharmonic effects; a larger $\delta\alpha_2$ means that the sample has stronger anharmonic effects. The standard deviation of α_2 shown in Fig. 4(b), for example, is $\delta\alpha_2 = 0.06$. $\delta\alpha_2$ is smaller at $T = 22$ and 34 °C [see Fig. 4(c)]. This trend is expected, since the

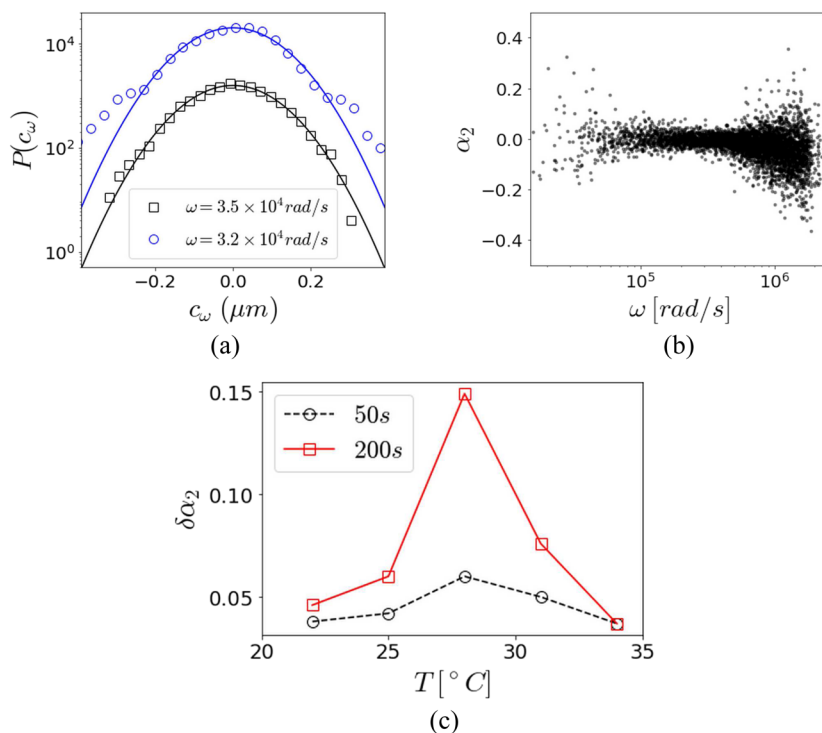


FIG. 4. (a) Probability distribution, $P(c_\omega)$, from two eigenfrequencies: $\omega = 3.5 \times 10^4$ (black square) and 3.2×10^4 (blue circle) rad/s. For clarity, data points of $\omega = 3.2 \times 10^4$ rad/s are multiplied by 10 (blue circle). The data are derived from a 50-s trajectory at $T = 28$ °C. The black and blue lines are Gaussian fits to the data; the non-Gaussian parameters are $\alpha_2 = 0.04$ (blue circle) and 0.02 (black square), respectively. (b) α_2 for different modes derived from a 50-s trajectory at $T = 28$ °C. (c) Standard deviation, $\delta\alpha_2$, vs T . The two sets of data are derived from 50-s (black circle) and 200-s (red square) trajectories, respectively.

latter two samples are glasses and are more dynamically arrested than the re-entrant supercooled liquid.

For trajectory durations up to 50 s, the harmonic approximation is easily satisfied for samples at all T 's. As a minor aside, if we increase the analysis trajectory duration to 200 s, then we observe an increased fraction of anharmonic modes at all T 's. This effect is apparent in the $\delta\alpha_2$ shown in Fig. 4(c). Interestingly, the increase in $\delta\alpha_2$ at $T = 28$ °C is significantly greater than those at 22 and 34 °C, implying a stronger connection between non-monotonic long-time relaxation and non-monotonic short-time anharmonic vibration.

We use 50-s particle trajectory data in all vibrational mode analyses. This probing time is significantly shorter than the α -relaxation time in these samples (>1000 s at $T = 28$ °C). Thus, the density of states obtained should be indistinguishable from that of an amorphous solid with the same equilibrium particle positions and potential energy landscape. Note that this equivalence of phonon behavior of a liquid vs an amorphous solid at times much shorter than the α -relaxation time of the liquid state has been confirmed by inelastic x rays and neutron scattering experiments.^{71–73} It is now well established, for example, that at sufficiently short time scales, liquids sustain longitudinal and transverse phonon modes.⁷⁴

D. Vibrational density of states

From the dynamical matrix based on the 50-s trajectory, we readily compute the vibrational spectrum of the sample at different T 's. We note that systematic errors arise in the computed ω due to finite sampling times. Specifically, the computed ω is accurate only when the number of independent image frames (f) is much greater

than the number of degrees of freedom.^{51,52,75} Thus, we employ well-known procedures to correct for these errors in ω . Briefly, we first calculate ω at several different values of f ranging between 5000 and 10 000 frames. We then obtain the more accurate (corrected) ω by linearly extrapolating the data to $1/f = 0$. Within our experimental accuracy, the resultant short-time density of states (DOS) scaled by frequency ω , i.e., $D(\omega)/\omega$, exhibits Debye model scaling at low frequencies (Fig. 5). Note that the accuracy of $D(\omega)/\omega$ decreases with decreasing ω and its uncertainty becomes fairly large for small ω 's.

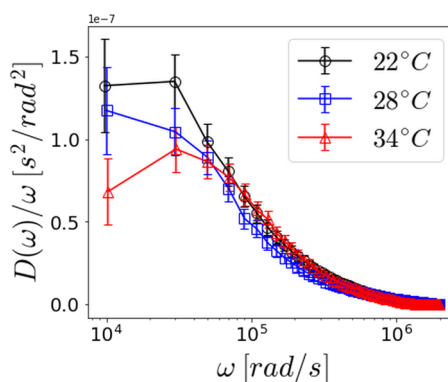


FIG. 5. Frequency-normalized vibrational density of states, $D(\omega)/\omega$, for the sample at $T = 22$, 28, and 34 °C. For clarity, data at 22 and 34 °C are very slightly shifted horizontally by -0.3×10^3 and 0.3×10^3 rad/s, respectively. The error bars indicate standard errors within each bin.

Thus, we cannot unambiguously discern a boson peak in the density of states. We do not fully understand the density of states at higher frequencies (e.g., $\omega > 10^5$ rad/s), which look somewhat similar even at different T 's; a better understanding of this phenomenon will require further study.

E. Effective spring constants

We extract the stiffness matrix $K = k_B T C^{-1}$ from the particle displacement covariance matrix C based on 50-s trajectory data. The effective spring constant between the i th and j th particles is defined as $k_{\text{eff}} = \partial^2 V / \partial r_{ij}^2$; here, V is the potential energy of the system, and $r_{ij} = [(x_i - x_j)^2 + (y_i - y_j)^2]^{1/2}$ is the separation between the two particles. We directly compute k_{eff} from the stiffness matrix K : the K matrix component associated with particle displacements along the x -axis is $K_{ij} = \partial^2 V / (\partial u_i \partial u_j) = \partial^2 V / (\partial x_i \partial x_j) = k_{\text{eff}} (\partial r_{ij} / \partial x_i) (\partial r_{ij} / \partial x_j) = -k_{\text{eff}} (x_i - x_j)^2 / r_{ij}^2$; similarly, the K matrix component associated with particle displacements along y -axis is $K_{N+i,N+j} = -k_{\text{eff}} (y_i - y_j)^2 / r_{ij}^2$. Thus, we obtain $k_{\text{eff}} = -K_{ij} - K_{N+i,N+j}$ directly from the K matrix.⁵⁷ This formula can be used to compute the k_{eff} between any pair of particles, although only particle pairs of nearest neighbors, i.e., $r_{ij} \lesssim \sigma_l$, have k_{eff} values above the noise level.

Figure 6 shows the measured k_{eff} at three temperatures $T = 22$, 28, and 34 °C (for clarity). Here, k_{eff} values are binned together based on r_{ij} , and the mean k_{eff} within each bin is plotted as a function of the bin center, r . Only k_{eff} from the nearest neighbors ($r/\sigma_s < 1.5$) are shown; k_{eff} at longer r are negligible. Like $g(r)$, $k_{\text{eff}}(r)$ also has three peaks. The most prominent peak is located around $r/\sigma_s \simeq 1.4$; this peak corresponds to the effective springs between large particles (large-large). The width of the large-large k_{eff} peak may be due to polydispersity in particle diameters or variation in their local packing fractions. When T increases, the large-large k_{eff} peak grows monotonically, indicating that stronger bonding arises between large particles due to stronger short-range attractive depletion forces. This observation is consistent with prior results from a bidisperse colloidal glass with a larger packing fraction, $\phi \simeq 0.82$.⁴² Recall also that the large-large particle correlation

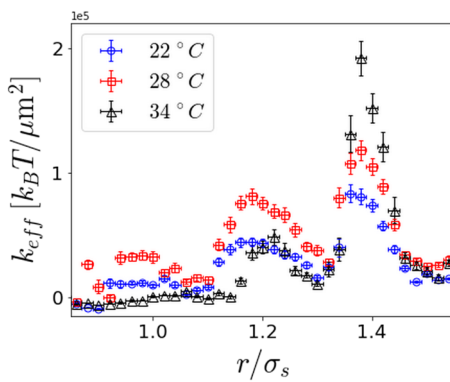


FIG. 6. Effective spring constant, k_{eff} , vs the equilibrium interparticle separation, r , at $T = 22$, 28, and 34 °C; r is normalized by σ_s . Horizontal and vertical error bars indicate the bin size and the standard deviation of k_{eff} within equal-sized (Δr) individual bins, respectively.

function peaks remain unchanged with increased attraction strength, i.e., the mean separation between large-large particle neighbors remains constant even as the attraction strength increases [see Fig. 2(b)].

The k_{eff} between small-particle pairs, with a peak at $r/\sigma_s \simeq 1$, differ from those of the large particle pairs. These k_{eff} are much smaller than the large-large k_{eff} , and interestingly, when T increases, the small-small k_{eff} first increase (from 22 to 28 °C) and then decrease (from 28 to 34 °C). Thus, the small-small k_{eff} exhibit a *non-monotonic* trend reminiscent of the widths of the small-small $g(r)$ peaks [see Fig. 2(b)].

F. Vibrational mode spatial extent and particle participation

The non-monotonic dependence of small-small particle k_{eff} vs depletion attraction strength indicates that small particles in the system experience and respond to the attractive depletion force differently than large particles. For example, with increasing depletion attraction, large particles move closer together (until contact) and experience a corresponding increase in k_{eff} . These differences in particle response lead to spatial heterogeneity of network stiffness and should modify network vibrational modes. Here, we investigate various properties associated with vibrational mode networks that may (or may not) be connected to the re-entrance effect; nevertheless, these properties about bidisperse glasses with short-range attraction are interesting in their own right and have not been reported.

To explore these questions further, we first examine the contributions of each particle type to each mode with frequency ω . We compute the participation fractions, $P_{F,l}(\omega) = \sum_{i=1}^{2N_l} \vec{e}_i(\omega)^2 + \vec{e}_{N_l+i}(\omega)^2$ for the large particles in each mode, and $P_{F,s} = \sum_{j=1}^{2N_s} \vec{e}_j(\omega)^2 + \vec{e}_{N_s+j}(\omega)^2$ for the small particles in each mode. Since $\vec{e}(\omega)$ is normalized, $P_{F,l} + P_{F,s} = 1$.

Figure 7 shows P_F data at $T = 22$, 28, and 34 °C, corresponding to the repulsive glass, liquid, and attractive glass, respectively. Since the low-frequency soft modes have been found to be related to particle rearrangements and long-time structural relaxation,^{59,60,76–78} we are especially interested in how these participation fractions change for the low-frequency modes with $\omega < 10^5$ rad/s. At 22 °C, we see that the large particles have higher participation fractions than the small particles in the low-frequency modes, but as the depletion attraction strength increases, the participation of small particles starts to rise and ultimately dominates the low-frequency modes at 34 °C. To illustrate the trend, we compute the mean low-frequency participation fraction, \bar{P}_F , from the first 200 low-frequency modes ($\omega < 10^5$ rad/s). Figure 7(d) shows \bar{P}_F vs T for both large and small particles. As T increases and the sample evolves from repulsive to attractive glass, the contributions of the large and small particles exhibit opposite trends. The participation fraction behaviors exhibit monotonic dependencies on T (depletion attraction strength); therefore, an obvious connection of this particular feature to the non-monotonic long-time structural dynamics is not apparent.

We next consider the degree of spatial extent of these modes. To this end, we compute the participation ratio, $P_r(\omega) = [\sum_{i=1}^{2N} |e_i(\omega)|^2]^2 / [2N \sum_{i=1}^{2N} |e_i(\omega)|^4]$. By convention, a mode is called localized (extended) if $P_r(\omega) < 0.2$ [$P_r(\omega) > 0.2$]. Figures 8(a) and

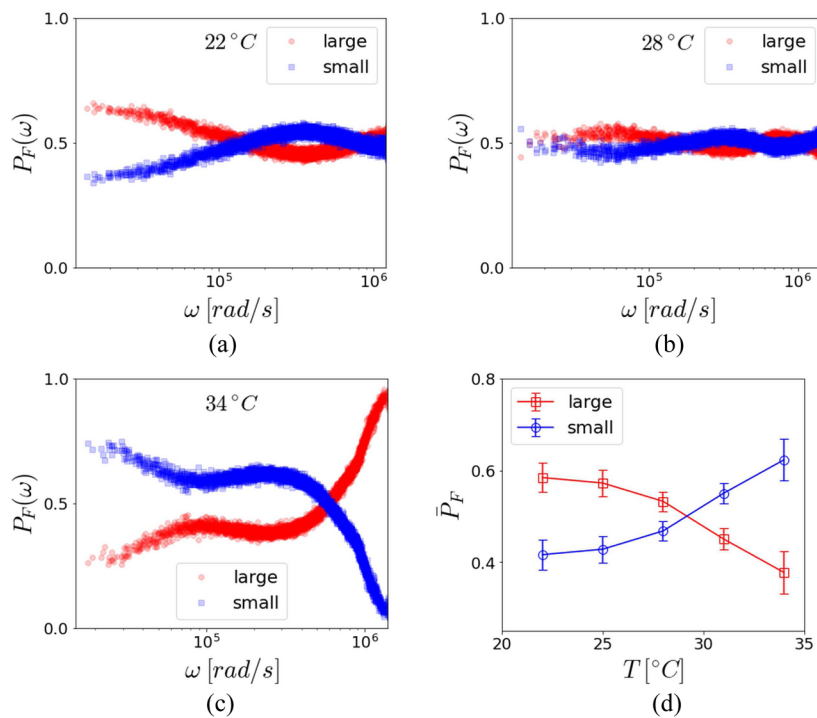


FIG. 7. Participation fraction, $P_F(\omega)$, of large (red circle) and small (blue square) particles at (a) $T = 22^\circ\text{C}$, (b) 28°C , and (c) 34°C . (d) Mean participation fraction, P_F , for the first 200 low-frequency modes ($\omega < 10^5$ rad/s).

8(b) show $P_r(\omega)$ measured at 22 and 34 °C, respectively. In the repulsive glass (22 °C), the low-frequency modes are mostly extended, but in the attractive glass (34 °C), the low-frequency modes are mostly localized. Figure 9(a) shows a low-frequency eigenvector in the repulsive glass corresponding to $\omega = 1.4 \times 10^4$ rad/s, which is marked by the gray bar in Fig. 8(a). Note that the individual particle displacement vectors exhibit long-wavelength-like, large-scale correlated motions, and the eigenmode involves more large particles.

A representative low-frequency eigenmode of the attractive glass, for contrast, is shown in Fig. 9(b). In this case, most of the particles show very small displacement and, thus, do not contribute much to the eigenmode motions. Amongst the participating particles, a few small particles dominate, i.e., a few small particles

show very large displacement amplitudes. We can understand these features in the context of our earlier observations about the local microstructure. The small particles have more free volume at high temperatures, probably due to compaction of aggregates of large particles. This increased local volume for small particles to “move within” is responsible for the soft modes at low frequencies in the attractive glass; these low-frequency modes are small-particle-rich and strongly localized. This idea also connects to the observations about participation fractions of small particles in the high-frequency modes of the attractive glass (i.e., $\omega > 10^6$ rad/s) [see Fig. 7(c)]; in this case, their contributions become very small, consistent with the decreasing small–small particle k_{eff} and a concomitant decrease in local rigidity. As was the case with the participation fractions, while the behaviors in the three states are distinctly different, an obvious

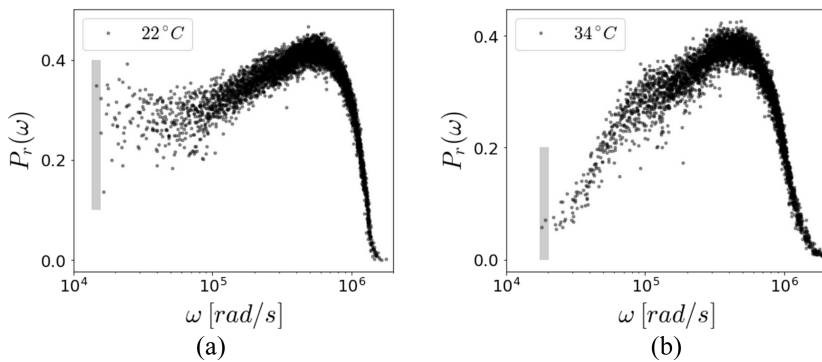


FIG. 8. Participation ratios $P_r(\omega)$ at (a) $T = 22^\circ\text{C}$ and (b) 34°C .

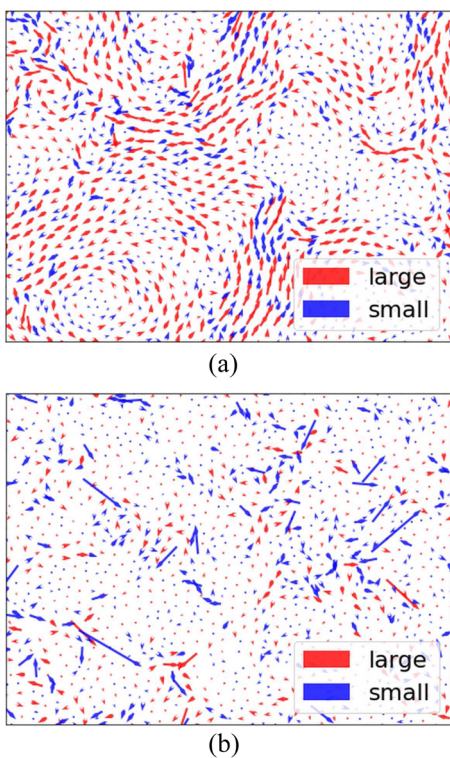


FIG. 9. Visualization of low-frequency eigenmodes at (a) $T = 22\text{ }^{\circ}\text{C}$ and (b) $34\text{ }^{\circ}\text{C}$; the corresponding ω for (a) and (b) are indicated by the gray bars in Figs. 8(a) and 8(b), respectively.

connection between mode extent and the non-monotonic long-time structural dynamics is not apparent.

IV. SUMMARY

We have experimentally investigated the structure and the short-time vibrational properties of 2D bidisperse colloidal glasses and supercooled liquids with temperature-tunable short-range depletion attraction. Importantly, the particle packing fraction in these samples is set so that the system experiences a re-entrant glass transition. The mean-square-displacements and self-intermediate scattering functions at long time-scales confirm the re-entrant glass transition, with dramatic non-monotonic spatiotemporal dynamics driven by an increasing (temperature-dependent) depletion attraction. To our knowledge, these are the first experiments reporting glass re-entrance phenomena involving bidisperse colloids.

Our bidisperse system differs qualitatively from the (predominantly) monodisperse systems employed in prior research on the re-entrance phenomenon. The bidisperse system has two particle species with a large diameter ratio (1:1.4) dispersed with approximately equal number density. As a result, the depletion attraction and its associated consequences experienced by the two particle types are different, and some of the microscopic features and mechanisms associated with the re-entrance phenomenon are new.

Our experiments focus on the structure and vibrational motion of particles within their nearest-neighbor cage. *A priori*, motions at these very short time and length scales might not be expected to be sensitive to re-entrance, since liquids and glasses are best distinguished by cage-breaking rather than in-cage motions. However, we found that the re-entrance phenomenon is accompanied by a non-monotonic change in the anharmonicity of the in-cage vibrational modes. Even at short time scales, the anharmonicity of the in-cage vibrations in the supercooled liquid is larger than that in the glass phase.

In addition, we analyzed the character of the predominantly harmonic vibrational modes vs depletion attraction strength, with attention to the size-dependent contributions of different particle species. We found that increasing depletion attraction strength induces non-monotonic changes in the effective spring constants between the small particles but not the large particles. The measured pair correlation functions revealed a non-monotonic variation in the local structure of the small particles too; again, this observation contrasts with the monotonic large particle behavior. Non-monotonic vs monotonic short-time vibrational properties, it seems, arise because the local structure and local stiffness entail a subtle interplay of small-particle interaction potentials and small-particle free volume that occur concurrently with increasing depletion attraction strength.

Looking forward, additional experiments are needed to determine the full phase behavior of 2D bidisperse colloidal suspensions with short-range attractions, e.g., as a function of ϕ , relative particle number density, and attraction strength. Our present studies suggest that the phase boundaries (e.g., for re-entrance) will depend on the particle-size-dependent local structures, local stiffness, and may be apparent in some aspects of the vibrational modes. In a related vein, it should be interesting to investigate intermediate time scales wherein particle vibrations exhibit significant anharmonic behaviors, e.g., using analysis methods that do not require the harmonic assumption,^{79–81} to fully link short-time harmonic vibrations to the α -relaxation at long times.

SUPPLEMENTARY MATERIAL

See the [supplementary material](#) for the *normal* MSDs and $F_s(\tau)$ s computed from particle displacements, Δr .

ACKNOWLEDGMENTS

We thank Kevin Aptowicz, Peter Collings, Remi Dreyfus, Sophie Ettinger, Analisa Hill, Michio Tanaka, and Wei-Shao Wei for helpful discussions. X.M., C.K.M., and A.G.Y. gratefully acknowledge financial support from the National Natural Science Foundation through Grant No. DMR2003659 and the Penn MRSEC grant (No. DMR1720530), including its Optical Microscopy Shared Experimental Facility.

DATA AVAILABILITY

The data that support the findings of this study are available from the corresponding author upon reasonable request.

REFERENCES

¹T. Eckert and E. Bartsch, "Re-entrant glass transition in a colloid-polymer mixture with depletion attractions," *Phys. Rev. Lett.* **89**, 125701 (2002).

²K. N. Pham, A. M. Puertas, J. Bergenholz, S. U. Egelhaaf, A. Moussaid, P. N. Pusey, A. B. Schofield, M. E. Cates, M. Fuchs, and W. C. K. Poon, "Multiple glassy states in a simple model system," *Science* **296**(5565), 104–106 (2002).

³W. C. K. Poon, "The physics of a model colloid polymer mixture," *J. Phys.: Condens. Matter* **14**(33), R859–R880 (2002).

⁴W. C. K. Poon, K. N. Pham, S. U. Egelhaaf, and P. N. Pusey, "Unsticking a colloidal glass, and sticking it again," *J. Phys.: Condens. Matter* **15**(1), S269–S275 (2002).

⁵C. K. Mishra, A. Rangarajan, and R. Ganapathy, "Two-step glass transition induced by attractive interactions in quasi-two-dimensional suspensions of ellipsoidal particles," *Phys. Rev. Lett.* **110**, 188301 (2013).

⁶C. K. Mishra, K. Hima Nagamanasa, R. Ganapathy, A. K. Sood, and S. Gokhale, "Dynamical facilitation governs glassy dynamics in suspensions of colloidal ellipsoids," *Proc. Natl. Acad. Sci. U. S. A.* **111**(43), 15362–15367 (2014).

⁷E. Zaccarelli and W. C. K. Poon, "Colloidal glasses and gels: The interplay of bonding and caging," *Proc. Natl. Acad. Sci. U. S. A.* **106**(36), 15203–15208 (2009).

⁸A. Latka, Y. Han, A. M. Alsayed, A. B. Schofield, A. G. Yodh, and P. Habdas, "Particle dynamics in colloidal suspensions above and below the glass-liquid re-entrance transition," *Europhys. Lett.* **86**(5), 58001 (2009).

⁹S. Mandal, S. Lang, M. Gross, M. Oettel, D. Raabe, T. Franosch, and F. Varnik, "Multiple re-entrant glass transitions in confined hard-sphere glasses," *Nat. Commun.* **5**(1), 4435 (2014).

¹⁰Z. Brown, M. J. Iwanicki, M. D. Gratale, X. Ma, A. G. Yodh, and P. Habdas, "Correlated rearrangements of disordered colloidal suspensions in the vicinity of the re-entrant glass transition," *Europhys. Lett.* **115**(6), 68003 (2016).

¹¹W. Götze, *Complex Dynamics of Glass-Forming Liquids: A Mode-Coupling Theory* (Oxford University Press, New York, 2008).

¹²E. Zaccarelli, H. Löwen, P. P. F. Wessels, F. Sciortino, P. Tartaglia, and C. N. Likos, "Is there a re-entrant glass in binary mixtures?," *Phys. Rev. Lett.* **92**, 225703 (2004).

¹³W. R. Chen, S. H. Chen, and F. Mallamace, "Small-angle neutron scattering study of the temperature-dependent attractive interaction in dense L64 copolymer micellar solutions and its relation to kinetic glass transition," *Phys. Rev. E* **66**, 021403 (2002).

¹⁴S. Karmakar, C. Dasgupta, and S. Sastry, "Short-time beta relaxation in glass-forming liquids is cooperative in nature," *Phys. Rev. Lett.* **116**, 085701 (2016).

¹⁵K. L. Ngai, "Relation between some secondary relaxations and the relaxations in glass-forming materials according to the coupling model," *J. Chem. Phys.* **109**(16), 6982–6994 (1998).

¹⁶C. K. Mishra, X. Ma, P. Habdas, K. B. Aptowicz, and A. G. Yodh, "Correlations between short- and long-time relaxation in colloidal supercooled liquids and glasses," *Phys. Rev. E* **100**, 020603 (2019).

¹⁷S. Asakura and F. Oosawa, "Interaction between particles suspended in solutions of macromolecules," *J. Polym. Sci.* **33**(126), 183–192 (1958).

¹⁸A. Vrij, "Polymers at interfaces and the interactions in colloidal dispersions," *Pure Appl. Chem.* **48**(4), 471–483 (1976).

¹⁹Y. Mao, M. E. Cates, and H. N. W. Lekkerkerker, "Depletion stabilization by semidilute rods," *Phys. Rev. Lett.* **75**, 4548–4551 (1995).

²⁰L.-J. Chen, S.-Y. Lin, C.-C. Huang, and E.-M. Chen, "Temperature dependence of critical micelle concentration of polyoxyethylenated non-ionic surfactants," *Colloids Surf., A* **135**(1–3), 175–181 (1998).

²¹R. Verma, J. C. Crocker, T. C. Lubensky, and A. G. Yodh, "Entropic colloidal interactions in concentrated DNA solutions," *Phys. Rev. Lett.* **81**, 4004–4007 (1998).

²²J. C. Crocker, J. A. Matteo, A. D. Dinsmore, and A. G. Yodh, "Entropic attraction and repulsion in binary colloids probed with a line optical tweezer," *Phys. Rev. Lett.* **82**, 4352–4355 (1999).

²³R. Verma, J. C. Crocker, T. C. Lubensky, and A. G. Yodh, "Attractions between hard colloidal spheres in semiflexible polymer solutions," *Macromolecules* **33**(1), 177–186 (2000).

²⁴M. Piech and J. Y. Walz, "Depletion interactions produced by nonadsorbing charged and uncharged spheroids," *J. Colloid Interface Sci.* **232**(1), 86–101 (2000).

²⁵K. Lin, J. C. Crocker, A. C. Zeri, and A. G. Yodh, "Colloidal interactions in suspensions of rods," *Phys. Rev. Lett.* **87**, 088301 (2001).

²⁶M. D. Gratale, T. Still, C. Matyas, Z. S. Davidson, S. Lobel, P. J. Collings, and A. G. Yodh, "Tunable depletion potentials driven by shape variation of surfactant micelles," *Phys. Rev. E* **93**, 050601 (2016).

²⁷A. D. Dinsmore, A. G. Yodh, and D. J. Pine, "Entropic control of particle motion using passive surface microstructures," *Nature* **383**(6597), 239–242 (1996).

²⁸P. D. Kaplan, J. L. Rouke, A. G. Yodh, and D. J. Pine, "Entropically driven surface phase separation in binary colloidal mixtures," *Phys. Rev. Lett.* **72**, 582–585 (1994).

²⁹A. D. Dinsmore, A. G. Yodh, and D. J. Pine, "Phase diagrams of nearly-hard-sphere binary colloids," *Phys. Rev. E* **52**, 4045–4057 (1995).

³⁰A. D. Dinsmore, P. B. Warren, W. C. K. Poon, and A. G. Yodh, "Fluid-solid transitions on walls in binary hard-sphere mixtures," *Europhys. Lett.* **40**(3), 337–342 (1997).

³¹A. D. Dinsmore, D. T. Wong, P. Nelson, and A. G. Yodh, "Hard spheres in vesicles: Curvature-induced forces and particle-induced curvature," *Phys. Rev. Lett.* **80**, 409–412 (1998).

³²K.-h. Lin, J. C. Crocker, V. Prasad, A. Schofield, D. A. Weitz, T. C. Lubensky, and A. G. Yodh, "Entropically driven colloidal crystallization on patterned surfaces," *Phys. Rev. Lett.* **85**, 1770–1773 (2000).

³³K. A. Dawson, "The glass paradigm for colloidal glasses, gels, and other arrested states driven by attractive interactions," *Curr. Opin. Colloid Interface Sci.* **7**(3–4), 218–227 (2002).

³⁴K. N. Pham, S. U. Egelhaaf, P. N. Pusey, and W. C. K. Poon, "Glasses in hard spheres with short-range attraction," *Phys. Rev. E* **69**, 011503 (2004).

³⁵H. N. W. Lekkerkerker and R. Tuinier, *Colloids and the Depletion Interaction* (Springer Netherlands, New York, 2011).

³⁶S. Buzzaccaro, R. Rusconi, and R. Piazza, "Sticky' hard spheres: Equation of state, phase diagram, and metastable gels," *Phys. Rev. Lett.* **99**, 098301 (2007).

³⁷M. Laurati, G. Petekidis, N. Koumakis, F. Cardinaux, A. B. Schofield, J. M. Brader, M. Fuchs, and S. U. Egelhaaf, "Structure, dynamics, and rheology of colloid-polymer mixtures: From liquids to gels," *J. Chem. Phys.* **130**(13), 134907 (2009).

³⁸M. Laurati, S. U. Egelhaaf, and G. Petekidis, "Nonlinear rheology of colloidal gels with intermediate volume fraction," *J. Rheol.* **55**(3), 673–706 (2011).

³⁹J. C. Conrad and J. A. Lewis, "Structure of colloidal gels during microchannel flow," *Langmuir* **24**(15), 7628–7634 (2008).

⁴⁰R. Pandey and J. C. Conrad, "Effects of attraction strength on microchannel flow of colloid-polymer depletion mixtures," *Soft Matter* **8**, 10695–10703 (2012).

⁴¹M. A. Lohr, T. Still, R. Ganti, M. D. Gratale, Z. S. Davidson, K. B. Aptowicz, C. P. Goodrich, D. M. Sussman, and A. G. Yodh, "Vibrational and structural signatures of the crossover between dense glassy and sparse gel-like attractive colloidal packings," *Phys. Rev. E* **90**, 062305 (2014).

⁴²M. D. Gratale, X. Ma, Z. S. Davidson, T. Still, P. Habdas, and A. G. Yodh, "Vibrational properties of quasi-two-dimensional colloidal glasses with varying interparticle attraction," *Phys. Rev. E* **94**, 042606 (2016).

⁴³X. Ma, J. Liu, Y. Zhang, P. Habdas, and A. G. Yodh, "Excess entropy and long-time diffusion in colloidal fluids with short-range interparticle attraction," *J. Chem. Phys.* **150**(14), 144907 (2019).

⁴⁴J. R. Savage, D. W. Blair, A. J. Levine, R. A. Guyer, and A. D. Dinsmore, "Imaging the sublimation dynamics of colloidal crystallites," *Science* **314**(5800), 795–798 (2006).

⁴⁵D. Heckendorf, K. J. Mutch, S. U. Egelhaaf, and M. Laurati, "Size-dependent localization in polydisperse colloidal glasses," *Phys. Rev. Lett.* **119**, 048003 (2017).

⁴⁶X. Ma, Z. S. Davidson, T. Still, R. J. S. Ivancic, S. S. Schoenholz, A. J. Liu, and A. G. Yodh, "Heterogeneous activation, local structure, and softness in supercooled colloidal liquids," *Phys. Rev. Lett.* **122**, 028001 (2019).

⁴⁷L. E. Silbert, A. J. Liu, and S. R. Nagel, "Vibrations and diverging length scales near the unjamming transition," *Phys. Rev. Lett.* **95**, 098301 (2005).

⁴⁸A. Ghosh, V. K. Chikkadi, P. Schall, J. Kurchan, and D. Bonn, "Density of states of colloidal glasses," *Phys. Rev. Lett.* **104**, 248305 (2010).

⁴⁹K. Chen, W. G. Ellenbroek, Z. Zhang, D. T. Chen, P. J. Yunker, S. Henkes, C. Brito, O. Dauchot, W. van Saarloos, A. J. Liu, and A. G. Yodh, "Low-frequency vibrations of soft colloidal glasses," *Phys. Rev. Lett.* **105**, 025501 (2010).

⁵⁰D. Kaya, N. L. Green, C. E. Maloney, and M. F. Islam, "Normal modes and density of states of disordered colloidal solids," *Science* **329**(5992), 656–658 (2010).

⁵¹S. Henkes, C. Brito, and O. Dauchot, "Extracting vibrational modes from fluctuations: A pedagogical discussion," *Soft Matter* **8**, 6092–6109 (2012).

⁵²K. Chen, T. Still, S. Schoenholz, K. B. Aptowicz, M. Schindler, A. C. Maggs, A. J. Liu, and A. G. Yodh, "Phonons in two-dimensional soft colloidal crystals," *Phys. Rev. E* **88**, 022315 (2013).

⁵³T. Still, C. P. Goodrich, K. Chen, P. J. Yunker, S. Schoenholz, A. J. Liu, and A. G. Yodh, "Phonon dispersion and elastic moduli of two-dimensional disordered colloidal packings of soft particles with frictional interactions," *Phys. Rev. E* **89**, 012301 (2014).

⁵⁴P. J. Yunker, Z. Zhang, M. Gratale, K. Chen, and A. G. Yodh, "Relationship between neighbor number and vibrational spectra in disordered colloidal clusters with attractive interactions," *J. Chem. Phys.* **138**(12), 12A525 (2013).

⁵⁵P. Keim, G. Maret, U. Herz, and H. H. von Grünberg, "Harmonic lattice behavior of two-dimensional colloidal crystals," *Phys. Rev. Lett.* **92**, 215504 (2004).

⁵⁶M. D. Gratale, P. J. Yunker, K. Chen, T. Still, K. B. Aptowicz, and A. G. Yodh, "Phonons in two-dimensional colloidal crystals with bond-strength disorder," *Phys. Rev. E* **87**, 052301 (2013).

⁵⁷W.-S. Wei, M. A. Gharbi, M. A. Lohr, T. Still, M. D. Gratale, T. C. Lubensky, K. J. Stebe, and A. G. Yodh, "Dynamics of ordered colloidal particle monolayers at nematic liquid crystal interfaces," *Soft Matter* **12**, 4715–4724 (2016).

⁵⁸Y. Zong, K. Chen, T. G. Mason, and K. Zhao, "Vibrational modes and dynamic heterogeneity in a near-equilibrium 2D glass of colloidal kites," *Phys. Rev. Lett.* **121**, 228003 (2018).

⁵⁹K. Chen, M. L. Manning, P. J. Yunker, W. G. Ellenbroek, Z. Zhang, A. J. Liu, and A. G. Yodh, "Measurement of correlations between low-frequency vibrational modes and particle rearrangements in quasi-two-dimensional colloidal glasses," *Phys. Rev. Lett.* **107**, 108301 (2011).

⁶⁰A. Ghosh, V. Chikkadi, P. Schall, and D. Bonn, "Connecting structural relaxation with the low frequency modes in a hard-sphere colloidal glass," *Phys. Rev. Lett.* **107**, 188303 (2011).

⁶¹T. E. Angelini, E. Hannezo, X. Trepat, M. Marquez, J. J. Fredberg, and D. A. Weitz, "Glass-like dynamics of collective cell migration," *Proc. Natl. Acad. Sci. U. S. A.* **108**(12), 4714–4719 (2011).

⁶²P. Das, H. G. E. Hentschel, E. Lerner, and I. Procaccia, "Robustness of density of low-frequency states in amorphous solids," *Phys. Rev. B* **102**, 014202 (2020).

⁶³H. Shen, P. Tan, and L. Xu, "Probing the role of mobility in the collective motion of nonequilibrium systems," *Phys. Rev. Lett.* **116**, 048302 (2016).

⁶⁴A. Baranyai and D. J. Evans, "Direct entropy calculation from computer simulation of liquids," *Phys. Rev. A* **40**, 3817–3822 (1989).

⁶⁵H. M. Ho, B. Lin, and S. A. Rice, "Three-particle correlation functions of quasi-two-dimensional one-component and binary colloid suspensions," *J. Chem. Phys.* **125**(18), 184715 (2006).

⁶⁶A. S.-Y. Sheu and S. A. Rice, "Transient ordering in a quasi-two-dimensional binary liquid near freezing," *J. Chem. Phys.* **129**(12), 124511 (2008).

⁶⁷B. Illing, S. Fritschi, H. Kaiser, C. L. Klix, G. Maret, and P. Keim, "Mermin-Wagner fluctuations in 2D amorphous solids," *Proc. Natl. Acad. Sci. U. S. A.* **114**(8), 1856–1861 (2017).

⁶⁸S. Vivek, C. P. Kelleher, P. M. Chaikin, and E. R. Weeks, "Long-wavelength fluctuations and the glass transition in two dimensions and three dimensions," *Proc. Natl. Acad. Sci. U. S. A.* **114**(8), 1850–1855 (2017).

⁶⁹Y. N. Ohshima and I. Nishio, "Colloidal crystal: Bead-spring lattice immersed in viscous media," *J. Chem. Phys.* **114**(19), 8649–8658 (2001).

⁷⁰C. Brito and M. Wyart, "Geometric interpretation of pre vitrification in hard sphere liquids," *J. Chem. Phys.* **131**(2), 024504 (2009).

⁷¹E. Burkel, "Phonon spectroscopy by inelastic x-ray scattering," *Rep. Prog. Phys.* **63**(2), 171–232 (2000).

⁷²S. Hosokawa, M. Inui, Y. Kajihara, K. Matsuda, T. Ichitsubo, W.-C. Pilgrim, H. Sinn, L. E. González, D. J. González, S. Tsutsui, and A. Q. R. Baron, "Transverse acoustic excitations in liquid Ga," *Phys. Rev. Lett.* **102**, 105502 (2009).

⁷³V. M. Giordano and G. Monaco, "Fingerprints of order and disorder on the high-frequency dynamics of liquids," *Proc. Natl. Acad. Sci. U. S. A.* **107**(51), 21985–21989 (2010).

⁷⁴K. Trachenko and V. V. Brazhkin, "Collective modes and thermodynamics of the liquid state," *Rep. Prog. Phys.* **79**(1), 016502 (2015).

⁷⁵M. Schindler and A. C. Maggs, "Truncated correlations in video microscopy of colloidal solids," *Soft Matter* **8**, 3864–3874 (2012).

⁷⁶M. L. Manning and A. J. Liu, "Vibrational modes identify soft spots in a sheared disordered packing," *Phys. Rev. Lett.* **107**, 108302 (2011).

⁷⁷J. Rottler, S. S. Schoenholz, and A. J. Liu, "Predicting plasticity with soft vibrational modes: From dislocations to glasses," *Phys. Rev. E* **89**, 042304 (2014).

⁷⁸M. Mosayebi, P. Ilg, A. Widmer-Cooper, and E. Del Gado, "Soft modes and nonaffine rearrangements in the inherent structures of supercooled liquids," *Phys. Rev. Lett.* **112**, 105503 (2014).

⁷⁹H. Tong and N. Xu, "Order parameter for structural heterogeneity in disordered solids," *Phys. Rev. E* **90**, 010401 (2014).

⁸⁰H. Tong, H. Hu, P. Tan, N. Xu, and H. Tanaka, "Revealing inherent structural characteristics of jammed particulate packings," *Phys. Rev. Lett.* **122**, 215502 (2019).

⁸¹X. Yang, H. Tong, W.-H. Wang, and K. Chen, "Emergence and percolation of rigid domains during the colloidal glass transition," *Phys. Rev. E* **99**, 062610 (2019).